Discontinuous Galerkin Methods for Multi-Material Shock Hydrodynamics

A. Pandare*, W. Li**, J. Waltz*, H. Luo**, and J. Bakosi*
Corresponding author: apandare@lanl.gov

* Los Alamos National Laboratory, USA.
** North Carolina State University, USA.

Abstract: This work establishes a DG method for three-dimensional multi-material flows, on unstructured tetrahedral meshes. A novel discontinuous Galerkin (DG) method with Hyperbolic-Tangent Interface Capturing (THINC) for the single-velocity multi-material (*two or more* materials) system is presented. The physical system considered here assumes stiff velocity relaxation, but no pressure and temperature equilibrium between the multiple materials. Second- and third-order DG methods are presented. A well-balanced DG discretization of the non-conservative system is proposed, and is verified by numerical test problems. To ensure strict conservation of material masses and total energy at the discrete level, a consistent interface strategy is implemented. Comparisons with the second-order finite volume method show that the DG method results in more accurate solutions for multi-material problems. With the help of numerical experiments, it is demonstrated that the DG method shows great potential in the field of multi-material hydrodynamics.

Keywords: Discontinuous Galerkin, Non-Equilibrium Multi-Material.

1 Introduction

Multi-material hydrodynamics has wide-ranging scientific and engineering applications from ICF and detonation studies to astrophysics. Resolving the multi-material interfaces constitutes a fundamental challenge in simulations of compressible multi-material phenomena. Consequently, over the years a large effort has concentrated on effectively resolving such interfaces. Diffuse interface methods (DIM) are one category of interface treatments that received wide acceptance due to its algorithmic simplicity. However, DIMs cause interfaces to smear over multiple computational cells; often in the order of dozens of cells for long simulation times. This is a major drawback of DIMs. Several research efforts were directed at using either compressive limiting strategies and/or aggressive interface reconstructions, that address this problem by "violating" TVD bounds in appropriate regions to obtain sharper interfaces. One such interface approach that algebraically reconstructs the volume-of-fluid (VOF or volume fraction) field is the THINC method [1]. THINC has the benefits of being algorithmically simple due to its purely algebraic and non-iterative nature (as opposed to geometric reconstructions), while being able to resolve material interfaces in 2-3 cells, regardless of cell-geometry [2, 3]. Recently, THINC has also been extended to be used with multiple materials [4]. Due to these reasons, THINC has great potential to be used in multi-material hydrodynamics.

Many multi-material problems involve large swaths of single material regions separated by such material interfaces. If sharp resolution of interfaces is retained through the simulation times, most of the computational domain is expected to be comprised of single material cells. To obtain highly accurate solutions in these single material regions, we propose the use of high-order DG. In this work, we present a high-order diffuse interface method for multi-material hydrodynamics. We combine the THINC reconstruction with the multi-material Discontinuous Galerkin (DG) discretization. This results in a method that benefits from the strengths of THINC and DG: 1) the DG high-order solution can compute highly accurate solutions in

Eleventh International Conference on
Computational Fluid Dynamics (ICCFD11),
Maui, HI, USA, July 11-15, 2022

ICCFD11-2501

smooth single material regions of the domain; 2) the interface capturing capabilities of THINC can resolve interfaces sharply *and* efficiently. A novel DG method for one-dimensional non-equilibrium multi-material hydrodynamics was recently proposed [5]. In this work, we extend this method to three-dimensional systems on unstructured meshes while combining it with THINC, and demonstrate the benefits for multi-material hydrodynamics.

2 Governing equations

The stiff velocity equilibrium limit of the multi-material hydrodynamics equations [6, 7] is considered here, with non-equilibrium pressures and temperatures. Finite-rate pressure relaxation is used to model physical pressure response of materials. The Eulerian form of this multi-material system of equations is,

$$\frac{\partial \boldsymbol{U}}{\partial t} + \frac{\partial \boldsymbol{F}_j}{\partial x_j} + \boldsymbol{D} = \boldsymbol{S}, \tag{1}$$

where,

$$\boldsymbol{U} = \begin{bmatrix} \alpha_k \\ \alpha\rho_k \\ \overline{\rho}u_i \\ \alpha\rho E_k \end{bmatrix}, \quad \boldsymbol{F}_j = \begin{bmatrix} 0 \\ \alpha\rho_k u_j \\ \overline{\rho}u_i u_j + \overline{p}\delta_{ij} \\ \alpha\rho H_k u_j \end{bmatrix}, \quad \boldsymbol{D} = \begin{bmatrix} u_j \frac{\partial\alpha_k}{\partial x_j} \\ 0 \\ 0 \\ Y_k u_j \frac{\partial\overline{p}}{\partial x_j} - u_j \frac{\partial(\alpha p_k)}{\partial x_j} \end{bmatrix}, \quad \boldsymbol{S} = \begin{bmatrix} S_{\alpha,k} \\ 0 \\ 0 \\ -\overline{p}S_{\alpha,k} \end{bmatrix}. \tag{2}$$

$k = 1, 2, ..., m$ is the material index, and m is the number of materials. Summation over repeating indices is implied, except for the material index k, where a summation will be explicitly stated when necessary. α_k, $\alpha\rho_k$, and $\alpha\rho E_k$ are the volume fraction, density and total energy of material k respectively. Bulk properties such as density $\overline{\rho}$, pressure $\overline{p}$, and internal energy $\overline{\rho e}$ are defined as,

$$\overline{\phi} = \sum_k \alpha_k \phi_k, \tag{3}$$

where ϕ_k is the material density ρ_k, material pressure p_k, or material internal energy ρe_k as required. The specific total energy of material k is, $E_k = e_k + u_j u_j/2$, and its specific total enthalpy is, $H_k = E_k + p_k/\rho_k$, where e_k is the specific internal energy of k. $Y_k = \alpha\rho_k/\overline{\rho}$ is the mass fraction of k. The source term $S_{\alpha,k}$ corresponds to the pressure relaxation via differential compaction of each material. It is defined as follows:

$$S_{\alpha,k} = \frac{1}{\tau}(p_k - p^*)\frac{\alpha_k}{\mathcal{K}_k}, \tag{4}$$

where p^* is the equilibrium pressure that the multi-material cell is expected to reach after sufficient time:

$$p^* = \frac{\sum_k \left(p_k \frac{\alpha_k}{\mathcal{K}_k}\right)}{\sum_k \frac{\alpha_k}{\mathcal{K}_k}}, \tag{5}$$

$\mathcal{K}_k = \rho_k a_k^2$ is the material's bulk modulus, and τ is the pressure-equilibration time-scale,

$$\tau = c_\tau \max_k \left(\frac{h}{a_k}\right). \tag{6}$$

This term models the material response to pressure by redistributing volume fractions based on material bulk modulii, resulting in a finite amount of relaxation between material pressures. For further details about the model, c.f. [8, 9]. For m materials, the above system has $(4m+3)$ unknowns in a three-dimensional case; $m \cdot [\alpha_k, \rho_k, p_k, E_k], u, v, w$. The system is composed of $(3m+3)$ equations. The additional m equations are obtained from the material equations of state, usually in the form of $p_k = p_k(\rho_k, e_k)$. This single-velocity multi-material system is hyperbolic [6, 7] with characteristic speeds u and $u \pm a_c$, where $a_c = \sqrt{(\sum_k \alpha\rho_k a_k^2)/\overline{\rho}}$ is the mixture speed of sound.

Eleventh International Conference on
Computational Fluid Dynamics (ICCFD11),
Maui, HI, USA, July 11-15, 2022

ICCFD11-2501

The system described above is similar to a stiff velocity relaxation limit of the Baer and Nunziato two-phase model [10, 11, 6, 12, 7]. The difference between these models is the pressure relaxation term. The finite pressure relaxation used here accounts for material properties while redistributing volumes as a response to pressure changes, rather than instantaneously relaxing the distinct material pressures. This results in a more physical depiction of energy distribution between materials with vastly different bulk modulii, for the problems of interest in this work.

2.1 Equations of state

For the purposes of demonstration, the stiffened-gas equation of state (SG-EoS) is used. However, the numerical method discussed here is not limited to this choice of EoS, and other EoS can be easily incorporated. The internal energy, temperature and speed of sound for material-k using the SG-EoS are given, respectively, as:

$$\rho e_k = \frac{p_k + P_{c_k}}{\gamma_k - 1} + P_{c_k}, \tag{7}$$

$$T_k = \left(\frac{\gamma_k}{\gamma_k - 1}\right)\frac{p_k + P_{c_k}}{\rho_k C_{p_k}}, \tag{8}$$

$$a_k = \sqrt{\gamma_k \frac{p_k + P_{c_k}}{\rho_k}}, \tag{9}$$

where P_{c_k}, γ_k, C_{p_k}, and T_k are the stiffness parameter, heat capacity ratio, specific heat at constant pressure, and temperature for material-k respectively.

3 The discontinuous Galerkin discretization

The discontinuous Galerkin discretization from [5] is used in this work. Consider a domain Ω with a closed boundary Γ on which Eq. (1) are to be solved. Ω is subdivided into finite elements $\Omega_e \in \Omega$, each with a boundary Γ_e. The semidiscrete form of Eq. (1) is,

$$
\begin{aligned}
&m_{\mu\nu}\frac{d(\alpha_k)_\nu}{dt} + \int_{\Gamma_e} \alpha_k u_j n_j B_\mu \mathrm{d}\Gamma - \int_{\Omega_e} \alpha_k \frac{\partial(u_j B_\mu)}{\partial x_j}\mathrm{d}\Omega = \int_{\Omega_e} S_{\alpha,k} B_\mu \mathrm{d}\Omega, \\
&m_{\mu\nu}\frac{d(\alpha\rho_k)_\nu}{dt} + \int_{\Gamma_e} \alpha\rho_k u_j n_j B_\mu \mathrm{d}\Gamma - \int_{\Omega_e} \alpha\rho_k u_j \frac{\partial B_\mu}{\partial x_j}\mathrm{d}\Omega = 0, \\
&m_{\mu\nu}\frac{d(\bar{\rho} u_i)_\nu}{dt} + \int_{\Gamma_e} \bar{\rho} u_i u_j n_j B_\mu \mathrm{d}\Gamma - \int_{\Omega_e} \bar{\rho} u_i u_j \frac{\partial B_\mu}{\partial x_j}\mathrm{d}\Omega = 0, \\
&m_{\mu\nu}\frac{d(\alpha\rho E_k)_\nu}{dt} + \int_{\Gamma_e} \alpha\rho H_k u_j n_j B_\mu \mathrm{d}\Gamma - \int_{\Omega_e} \alpha\rho H_k u_j \frac{\partial B_\mu}{\partial x_j}\mathrm{d}\Omega \\
&\quad - \int_{\Omega_e} u_j \frac{\partial(\alpha p_k)}{\partial x_j} B_\mu \mathrm{d}\Omega + \int_{\Omega_e} Y_k u_j \frac{\partial\bar{p}}{\partial x_j} B_\mu \mathrm{d}\Omega = -\int_{\Omega_e} \bar{p} S_{\alpha,k} B_\mu \mathrm{d}\Omega.
\end{aligned}
\tag{10}
$$

where U_μ are the N unknown coefficients of the high-order polynomial U. Dubiner polynomials [13, 14] are used as the solution basis here. The Greek alphabet is specifically used as a modal index to help avoid confusion with directional indices (i, j). Surface and volume integrals are computed using Gaussian quadrature of appropriate order of accuracy. Surface fluxes at quadrature points are approximated by the AUSM$^+$-up scheme [15]. Integrals of non-conservative products are computed in a manner compatible with the surface flux terms, as concluded by Abgrall and Saurel [16, 11]. An explicit three-stage third-order TVD Runge-Kutta method [17] is used to discretize (10) in time. Further details can be found in [5].

3.1 Limiting

Limiting is used to maintain stability in regions where the solution becomes discontinuous. The spectral decay indicator [18] is used to detect such discontinuities. The spectral decay function is given as:

$$\eta_k = \frac{\int_{\Omega_e} \left((\alpha_k \rho_k)_p - (\alpha_k \rho_k)_{p-1}\right)^2}{\int_{\Omega_e} (\alpha_k \rho_k)_p^2} \tag{11}$$

$$\eta = \max_i \eta_k \tag{12}$$

where k is the material index, and $\cdot_p$ and $\cdot_{p-1}$ are the polynomial solutions of pth and $p-1^{th}$ order. Elements with $\eta > 10^{-5.7}$ are marked for limiting. Limiting is only used in elements where discontinuities are detected. Once a troubled element is detected, the 3rd order terms are dropped from the DG expansion, and only the 2nd order DG coefficients are limited using a vertex-based limiter [19]. Since the limiter does not affect solutions otherwise, the method can retain high-order accuracy in smooth regions. An example of shock detection for the triple-point problem is shown in Fig. 1.
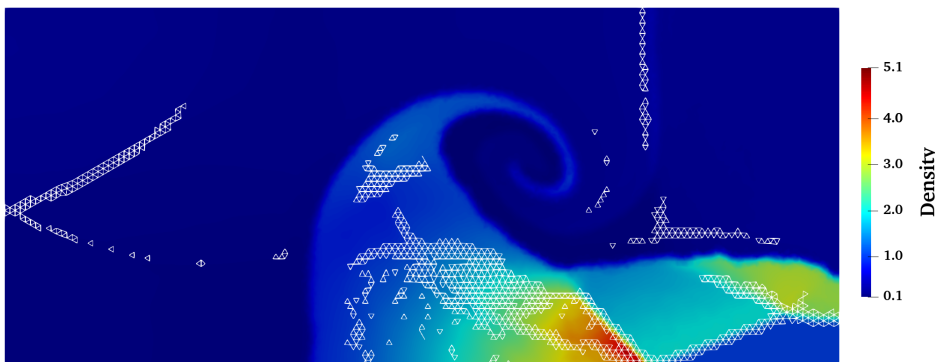
Figure 1: Density for triple-point; elements with discontinuities detected by spectral-decay indicator highlighted

3.2 THINC reconstruction with DG discretization

The Tangent of Hyperbola for Interface Capturing (THINC) [1, 2] approach is used for problems with sharp material interfaces. In this case, the volume fraction values at quadrature points are determined from the THINC reconstruction, rather than the DG polynomial solution. The following condition is used to detect if an element Ω_e lies within a material interface:

$$\epsilon < \left(\int_{\Omega_e} \alpha_k d\Omega\right) < (1 - \epsilon), \qquad \epsilon = 10^{-8}. \tag{13}$$

This ensures retention of sharp interfaces. For problems with sharp interfaces, this is the same as using a second-order FV scheme for volume fraction equations, while using high-order DG for the rest of the equations in the system. This is actually ideal, since high-order methods have little benefit in capturing discontinuities. Therefore switching to FV for the volume fraction equations (which only have discontinuities, not smooth variations) saves some computational effort.

For multi-material (> 2) interfaces, a modified THINC reconstruction [4] is used. The basic idea of this modification is to drop the value of the steepness parameter β when more than two materials with volume fractions of more than 2.5% are detected in a cell. This drop is achieved by linearly varying β from 2.5 to 1.5 between volume fractions of 2.5% to 5% for the third material in the computational cell. Further details and discussion can be found in [4]. Shyue and Xiao's interface treatment [20] is used to maintain consistency between reconstructions of volume fraction and other quantities such as $\alpha\rho_k$, $\alpha\rho E_k$ in interface elements.

4   Numerical studies

The multi-material DG method has been implemented in Quinoa, a distributed memory parallel code with automatic dynamic load balancing (see `https://quinoacomputing.github.io`). We now present numerical solutions to a few benchmark problems to verify the THINC-DG method. Where applicable, L_2-norms of errors are used. The minimum volume fraction of $\epsilon_M = 10^{-12}$ is used to represent non-existent materials in single material regions. A material indicator function defined as $\sum_k \alpha_k k$ is used to visualize material volume fractions, which is useful for problems with more than two materials. Tetrahedral meshes are used for all the test problems.

4.1   Manufactured solution: advection of equilibrium interface

A manufactured solution problem is developed for the multi-material system of equations using the method described in [21]. Since this problem is smooth, it is used to verify the order of accuracy of the DG method. THINC reconstruction is not used for this problem, since the interfaces are not sharp by design, so as to allow order-of-accuracy studies. The analytical solution for this problem is:

$$
\begin{pmatrix} \alpha_1 \\ \rho_k \\ u_j \\ p_k \\ \rho e_k \end{pmatrix} = \begin{pmatrix} \frac{1}{2}\left(1.0 - \tanh\left(10((x-x_c(t)) + (y-y_c(t)) + (z-z_c(t)))\right)\right) \\ x + y + z + 5.0 \\ (3,2,1) \\ p_0 \\ (p_0(\gamma_k - 1))^{-1} \end{pmatrix}
\tag{14}
$$

where, $x_c(t) = x_0 + u_1 t$, and so on, and $x_0 = y_0 = z_0 = 0.45$. The source-terms for this manufactured solution are:

$$
\begin{pmatrix} s_{\alpha_k} \\ s_{\rho_k} \\ s_{u_j} \\ s_{E_k} \end{pmatrix} = \begin{pmatrix} 0 \\ \sum_j u_j s_{\alpha_k} \\ u_j(s_{\rho_1} + s_{\rho_2}) \\ \frac{1}{2} u_j u_j s_{\rho_k} \end{pmatrix}
\tag{15}
$$

Here $p_0 = 0.4$. A one-dimensional representation of the partial material densities and bulk density for this problem is shown in Fig. 2. Both material partial densities have non-linear distributions, making this problem ideal for testing the order-of-accuracy.
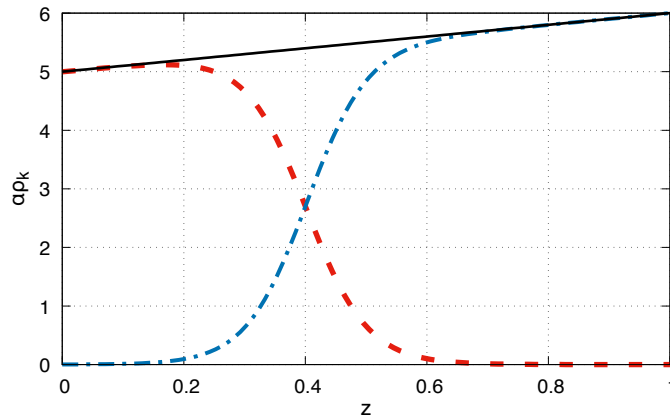
Figure 2: Material density and bulk density distributions for the manufactured solution problem

An order of accuracy study was performed on 3D tetrahedral meshes for the 2nd and 3rd order multi-material DG method. A set of meshes with 35974, 287792, 2302336, and 18418688 tetrahedra was used.

Eleventh International Conference on
Computational Fluid Dynamics (ICCFD11),
Maui, HI, USA, July 11-15, 2022

ICCFD11-2501

The L_2 norms of errors in $\alpha\rho_k$ for each of these meshes (max. edge length Δx) using DG(P_1) and DG(P_2) are shown in the table below. The two methods demonstrate design order-of-accuracy, as shown in Fig. 3. Second and third order lines are shown for reference.

Δx	$NDOF_{P1}$	$\log \|e\|_{P1}$	$NDOF_{P2}$	$\log \|e\|_{P2}$
0.042752	143896	7.911897e-03	359740	6.022763e-04
0.021376	1151168	1.920980e-03	2877920	7.408737e-05
0.010688	9209344	4.694062e-04	23023360	9.095131e-06
0.005344	73674752	1.159295e-04	184186880	1.120956e-06

Table 1: L2-norms of errors in solution $(\alpha\rho_k)$ using DG(P$_1$) and DG(P$_2$)
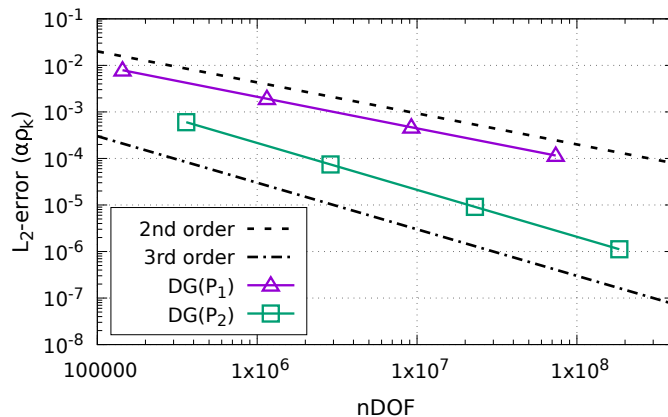
Figure 3: Error reduction with mesh refinement for 2nd and 3rd order multi-material DG

4.2   Osher-Shu shock-entropy wave interaction test problem for two materials

The the two material version of Osher-Shu's shock-entropy wave problem [22] is used to assess performance of the DG method as compared to the second order FV method (FV2). The initial conditions are:

$$\left(\alpha_1, \alpha_2, u, \rho_k, p_k\right) = \begin{cases} \epsilon_M, \ (1.0 - \epsilon_M), \ 2.6294, \ 3.8571, \ 10.3333 & \text{for } x \leq -4 \\ (1.0 - \epsilon_M), \ \epsilon_M, \ 0, \ 1 + 0.2\sin(5x), \ 1.0 & \text{for } x > -4. \end{cases}$$

A tetrahedral mesh with 22,400 elements (average edge length 0.03563) is used. The domain spans $-5 \leq x \leq 5$, with two layers of elements in the y and z directions. The THINC-FV2 and THINC-DG(P_1) methods are compared in this test. Material indicator profiles at final time $t = 1.8$ are shown in Fig. 4. The left figure shows the contour plot using THINC-DG(P_1) on the 3D mesh. The right figure shows the material indicator profile along the domain center line and compares the cell-average material indicators obtained by the THINC methods with a DG method that does not use THINC. The advantages of using THINC are clear from this plot. Both THINC methods are able to capture the material interface in 2-3 elements, as opposed to 6-7 cells when THINC is not used. Since the interface is only 2-3 cells wide, the first-order approximation from [20] is applied to a very narrow band of cells. Thus, the accuracy in the majority of the domain is unaffected.
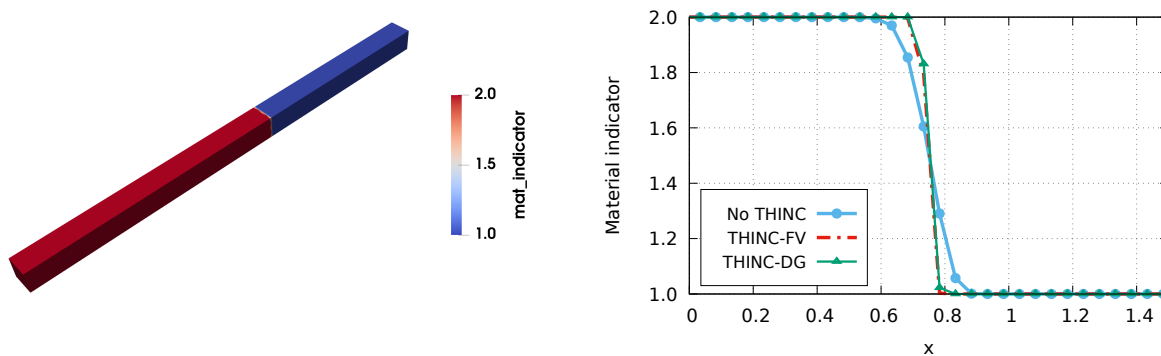
Figure 4: Material indicator function for the two material shock-entropy wave interaction problem: contour plot (left), line plot zoomed in at the interface location (right)
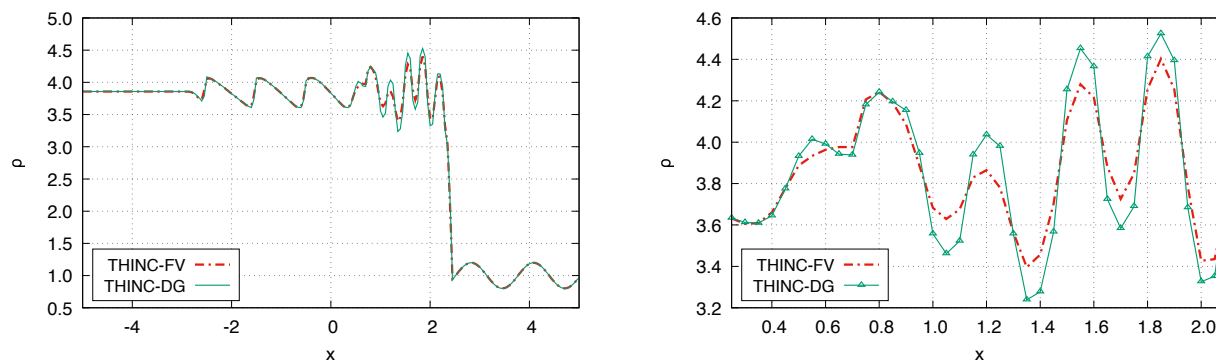
Figure 5: Mixture density (left) for the shock-entropy wave problem obtained by the two methods; closer view of the high-gradient zone (right)

This is confirmed in the density profiles shown in Fig. 5. The oscillatory behavior of this problem downstream of the shock is captured very sharply by the THINC-DG method as compared to the THINC-FV method; thereby highlighting the usefulness of the DG method. The multi-material nature of the problem only shows in the narrow band of interface cells, while in the rest of the domain the high-accuracy of the DG method is retained.

4.3 Triple point problem

The multi-material triple point problem [23] is a standard benchmark test used to verify hydro-methods. This problem involves three materials and a pressure-jump between two of these. Zones for the initial conditions are shown in Fig. 6. These zones are initialized as:

$$
\left(\alpha_1, \alpha_2, \alpha_3, u, p_k, T_k\right) = \begin{cases} (1.0 - 2\epsilon_M), \epsilon_M, \epsilon_M, 0 \text{ m/s}, 1.0, 4.3554007 \times 10^{-4} & \text{for zone } \mathcal{A} \\ \epsilon_M, (1.0 - 2\epsilon_M), \epsilon_M, 0 \text{ m/s}, 0.1, 3.4843206 \times 10^{-4} & \text{for zone } \mathcal{B} \\ \epsilon_M, \epsilon_M, (1.0 - 2\epsilon_M), 0 \text{ m/s}, 0.1, 3.4843206 \times 10^{-4} & \text{for zone } \mathcal{C}. \end{cases}
$$

with the EoS parameters for the three materials as:

Eleventh International Conference on
Computational Fluid Dynamics (ICCFD11),
Maui, HI, USA, July 11-15, 2022

ICCFD11-2501

Material	γ	P_c (Pa)	C_p (J/K)
1	1.5	0	4592.0
2	1.4	0	1004.5
3	1.5	0	4592.0

This gives densities of 1, 1, and 0.125 in zones $\mathcal{A}$, $\mathcal{B}$, and $\mathcal{C}$ respectively. A large amount of vorticity is generated at the intersection of the three interfaces causing a roll-up, thereby making this problem a good test of interface reconstruction capabilities of the method.
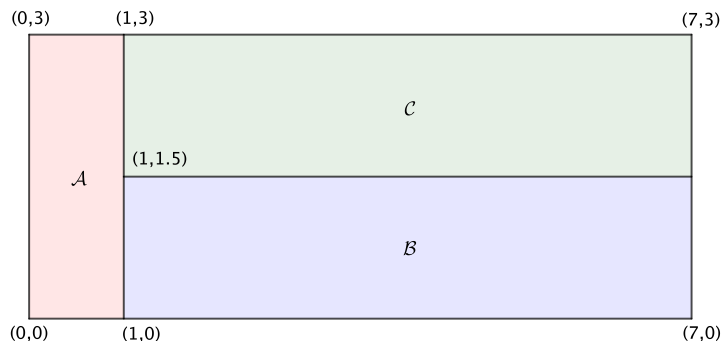
Figure 6: Initial conditions for the triple-point problem

First, the effect of THINC reconstruction is shown in Fig. 7. Both results in Fig. 7 are obtained using an FV scheme on the same mesh. The difference between the two calculations is that one does not use THINC for interface treatment, while the other does. If an interface reconstruction technique is not used for this problem, the interfaces get extremely distorted due to numerical dissipation. On the other hand, when THINC is used, the interfaces are resolved sharply.
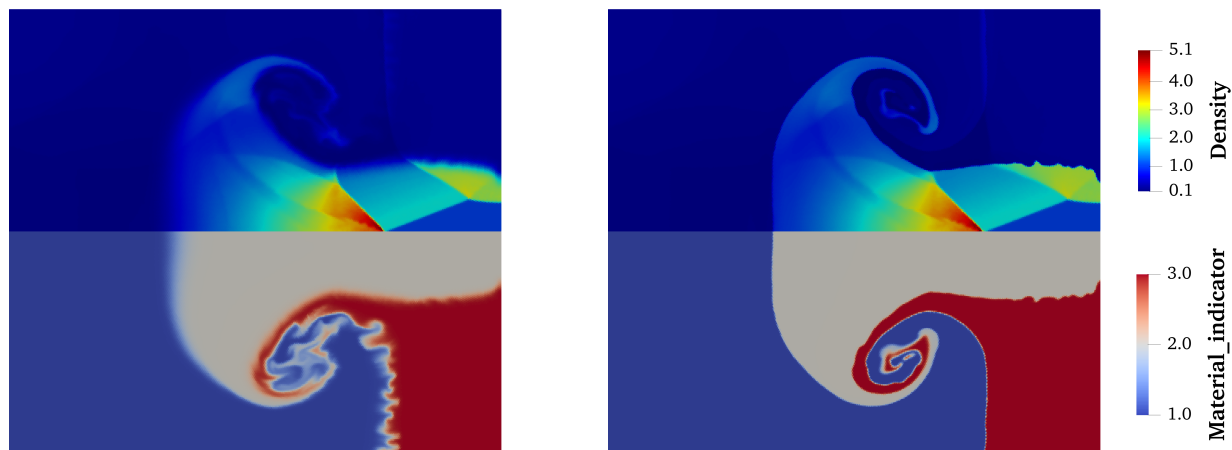
Figure 7: Bulk density (top planes) and material indicator (bottom planes) function for the triple-point problem; *left:* without THINC reconstruction, *right:* with THINC reconstruction

Now, the THINC-FV2 and THINC-DG(P_1) are compared on the same mesh. A mesh with 165,712 tetrahedra is used. It has two layers of elements in the z direction, and an average edge length of 0.051195.

Eleventh International Conference on
Computational Fluid Dynamics (ICCFD11),
Maui, HI, USA, July 11-15, 2022

ICCFD11-2501

Density and x-velocity plots along the domain symmetry axis are shown in Fig. 8. The shock is captured more sharply by THINC-DG as compared to THINC-FV.
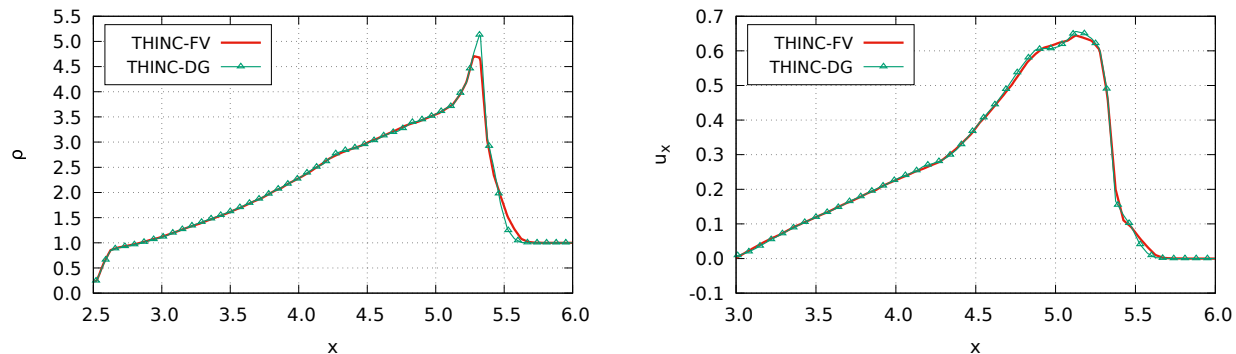
Figure 8: Density (left) and x-velocity (right) for the triple-point problem obtained by FV2 and DG(P_1) along the domain symmetry-axis

4.4 Shock He-bubble interaction problem

The shock-Helium bubble interaction problem has been used [24, 23] to study the interface capturing capabilities of numerical methods after shock impact. A Mach 1.22 shock strikes a Helium bubble with radius 2.5 cm. The problem is solved on a domain [0 m, 0.2225 m] × [0 m, 0.0445 m] × [0 m, 0.0445 m], with the bubble centered at $(0.1725, 0.0, 0.0)$. The initial conditions are:

$$(\alpha_1, \alpha_2, u, p_k, T_k) = \begin{cases} \epsilon_M, (1.0 - \epsilon_M), -113.5 \text{ m/s}, 1.5698 \times 10^5 \text{ Pa}, 283.86 \text{ K} & \text{for } x \geq 0.2125 \text{ m} \\ \epsilon_M, (1.0 - \epsilon_M), 0 \text{ m/s}, 10^5 \text{ Pa}, 248.88 \text{ K} & \text{for } x < 0.2125 \text{ m}. \end{cases}$$

The bubble is initialized in the region $(x - 0.1725)^2 + y^2 + z^2 < (0.025 \text{ m})^2$: with $\alpha_1 = (1.0 - \epsilon_M)$ and $\alpha_2 = \epsilon_M$. Initial conditions are also shown in Fig. 9, where $\mathcal{L}$ and $\mathcal{R}$ represent the pre- and post-shock states respectively. The EoS parameters for this test are:

Material	γ	P_c (Pa)	C_p (J/K)
1 (Helium)	1.648	0	5192.6
2 (Air)	1.4	0	1004.5
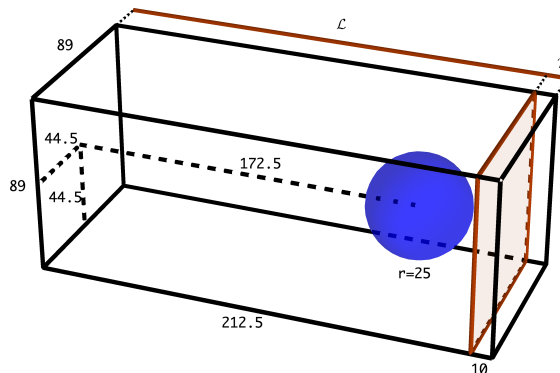
Figure 9: Initial conditions for the shock He-bubble interaction. All dimensions in mm.

A coarse mesh with 258,157 tetrahedra (average edge-length 0.002606) is used. The density and material indicator contours are shown in Fig. 10, with a surface contour of the bubble ($\alpha_1 = 0.5$). Sharp interface capturing is observed from the material indicator contours. Interface fragmentation is observed, as in the experiments.
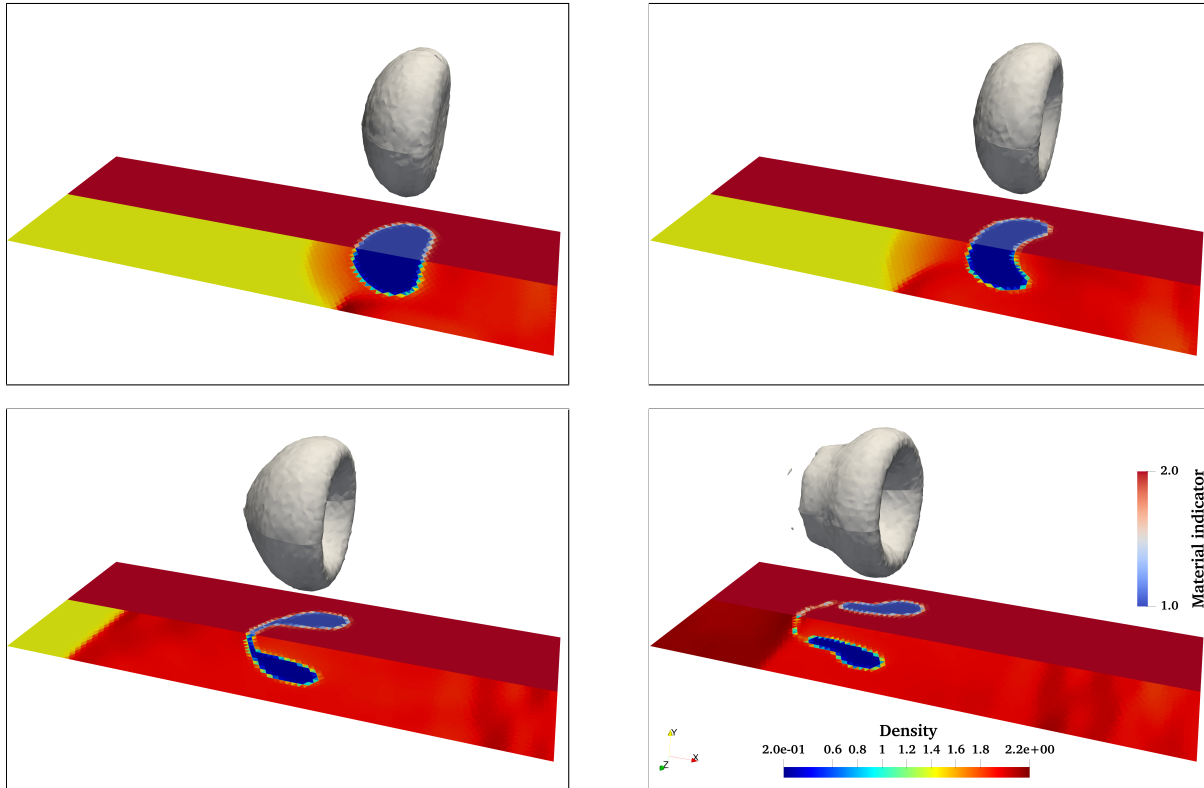
Figure 10: Bulk density (front cut-plane) and material indicator (rear cut-plane) contours for the shock He-bubble interaction test at $t = 169$ μs, $t = 246$ μs, $t = 455$ μs, and $t = 731$ μs, from left to right and top to bottom.

Pressure profiles obtained by THINC-FV2 and THINC-DG(P_1) along the center axis of the domain, and along an axis offset from the center by $[0.0225, 0.0225]$ in the y and z directions are shown in Figs. 11 and 12 respectively. The fluctuations (peaks and troughs) in the transmitted and reflected shocks and rarefactions are captured more accurately by DG as compared to FV. Density profiles at $t = 360$ μs along the centerline are shown in Fig. 13. The initial density profile along the same line is also shown in dotted lines, where the Helium bubble is visible as a region of low density. At the time instant shown, the bubble is close to collapse, and the shock and rarefaction waves have been transmitted out of the bubble. DG(P_1) shows some improvements in capturing the peak of the shock.

However, the benefits from DG(P_1) are limited, especially considering the increase in computational effort from FV2. One of the reasons this might be the case, is the ineffectiveness of the shock detector. It is observed that the shock detector marks most elements for limiting, except the ones with constant states (see Fig. 14). This behavior will lead to reduced accuracy in smooth regions of the flow. A third-order DG(P_2) method might also lead to better gains in accuracy, despite even higher computational cost increases. These topics will be studied in a future work.
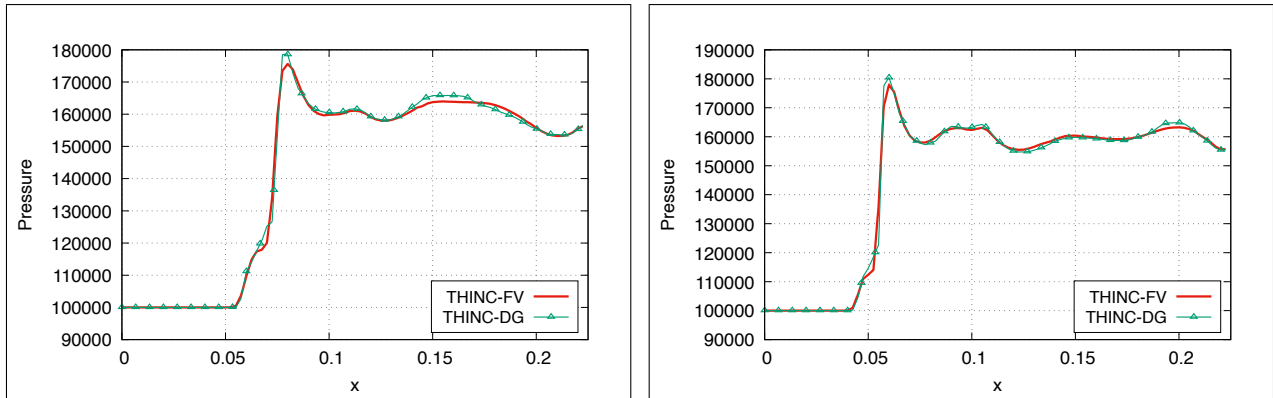
Figure 11: Pressure profiles at center axis using FV2 and DG(P1) at 360 μs and 400 μs
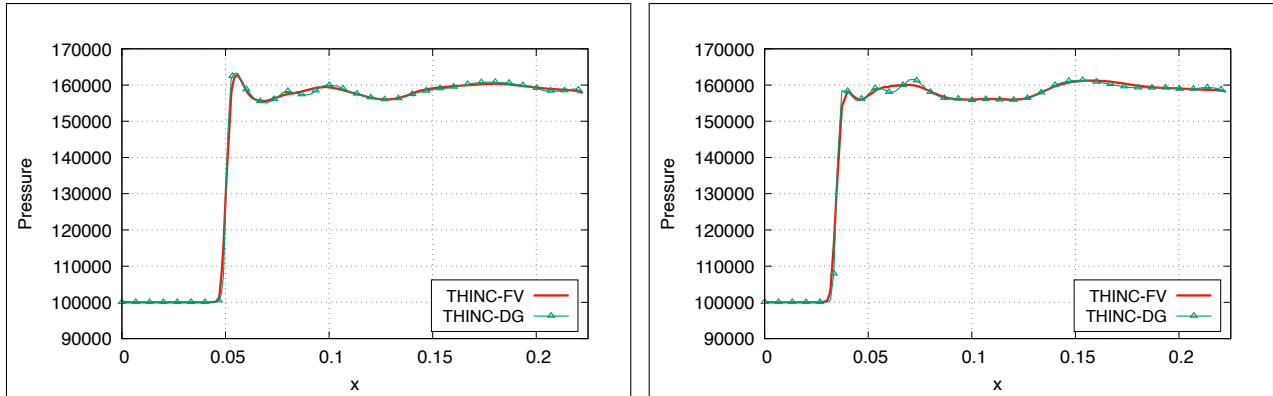
Figure 12: Pressure profiles at offset axis using FV2 and DG(P1) at 400 μs and 440 μs
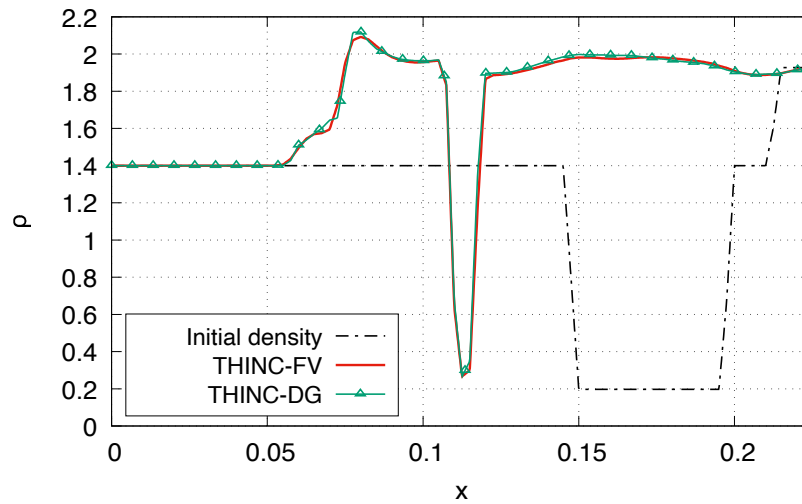
Figure 13: Densities obtained by FV2 and DG(P1) along the domain center-axis at 360 μs
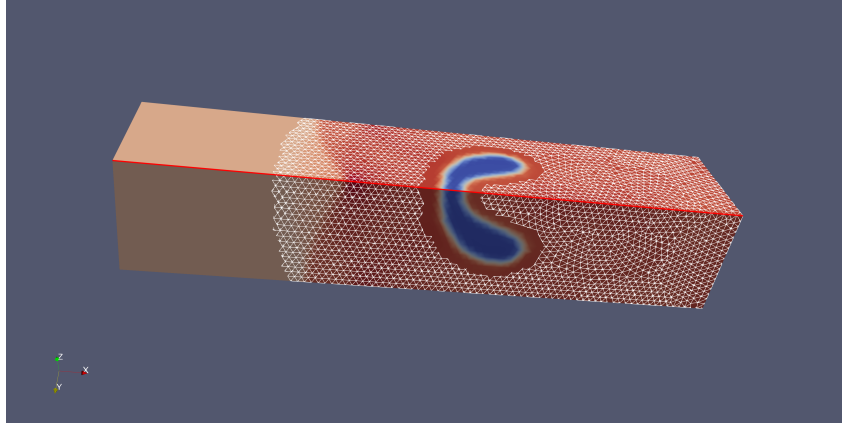
Figure 14: Density at 360 μs, detected "troubled" cells highlighted; central axis of bubble in red

5   Summary and conclusions

A THINC-DG method for multi-material hydrodynamics is proposed in this work. The method leverages the strengths of the THINC and DG methods, resulting in a high-order multi-material method that: i) can compute highly accurate solutions in smooth single material regions of the problem domain, and ii) can maintain sharp multi-material interface resolution efficiently. The proposed method is verified with the help of a few numerical tests, that also demonstrate the accuracy of the method. Based on the results, the THINC-DG method shows potential to be used for multi-material hydrodynamics simulations.

However, further research on shock detectors for multi-material flows is needed to maximize gains from the DG methods. Studies and comparisons of various available shock detectors are a topic of ongoing work. Using AMR will allow use of coarser mesh elements in single material regions and refine around material interfaces, thereby leveraging the benefits of DG. This will be explored in future work. Further V&V is of interest and will be reported in a future publication.

Acknowledgments

References

[1] F. Xiao, Y. Honma, and T. Kono. A simple algebraic interface capturing scheme using hyperbolic tangent function. *International Journal for Numerical Methods in Fluids*, 48(9):1023–1040, 2005.

[2] S. Ii, B. Xie, and F. Xiao. An interface capturing method with a continuous function: The THINC method on unstructured triangular and tetrahedral meshes. *Journal of Computational Physics*, 259:260–269, 2014.

[3] L. Li, R. Löhner, A. K. Pandare, and H. Luo. A vertex-centered finite volume method with interface sharpening technique for compressible two-phase flows. *Journal of Computational Physics*, 460:111194, 2022.

[4] A. K. Pandare, J. Waltz, and J. Bakosi. Multi-material hydrodynamics with algebraic sharp interface capturing. *Computers & Fluids*, 215:104804, 2021.

Eleventh International Conference on
Computational Fluid Dynamics (ICCFD11),
Maui, HI, USA, July 11-15, 2022

ICCFD11-2501

[5] A. K. Pandare, J. Waltz, and J. Bakosi. A reconstructed discontinuous Galerkin method for multi-material hydrodynamics with sharp-interfaces. *International Journal for Numerical Methods in Fluids*, 92:874–898, 2020.

[6] A. K. Kapila, R. Menikoff, J. B. Bdzil, S. F. Son, and D. S. Stewart. Two-phase modeling of deflagration-to-detonation transition in granular materials: Reduced equations. *Physics of fluids*, 13(10):3002–3024, 2001.

[7] M. Pelanti and K-M. Shyue. A numerical model for multiphase liquid–vapor–gas flows with interfaces and cavitation. *International Journal of Multiphase Flow*, 113:208–230, 2019.

[8] M. Shashkov. Closure models for multimaterial cells in arbitrary Lagrangian—Eulerian hydrocodes. *International Journal for Numerical Methods in Fluids*, 56(8):1497–1504, 2008.

[9] V. A. Dobrev, T. V. Kolev, R. N. Rieben, and V. Z. Tomov. Multi-material closure model for high-order finite element Lagrangian hydrodynamics. *International Journal for Numerical Methods in Fluids*, 82(10):689–706, 2016.

[10] M. R. Baer and J. W. Nunziato. A two-phase mixture theory for the deflagration-to-detonation transition (DDT) in reactive granular materials. *International Journal of Multiphase Flow*, 12(6):861–889, 1986.

[11] R. Saurel and R. Abgrall. A multiphase Godunov method for compressible multifluid and multiphase flows. *Journal of Computational Physics*, 150(2):425–467, 1999.

[12] R. Saurel, F. Petitpas, and R. A. Berry. Simple and efficient relaxation methods for interfaces separating compressible fluids, cavitating flows and shocks in multiphase mixtures. *journal of Computational Physics*, 228(5):1678–1712, 2009.

[13] H. Luo and C. Pozrikidis. A Lobatto interpolation grid in the tetrahedron. *IMA journal of applied mathematics*, 71(2):298–313, 2006.

[14] J. Hesthaven and T. Warburton. *Nodal discontinuous Galerkin methods: algorithms, analysis, and applications.* Springer Science & Business Media, 2008.

[15] M-S. Liou. A sequel to AUSM, part II: AUSM+-up for all speeds. *Journal of Computational Physics*, 214(1):137–170, 2006.

[16] R. Abgrall. How to prevent pressure oscillations in multicomponent flow calculations: a quasi conservative approach. *Journal of Computational Physics*, 125(1):150–160, 1996.

[17] S. Gottlieb and C-W. Shu. Total variation diminishing Runge-Kutta schemes. *Mathematics of computation of the American Mathematical Society*, 67(221):73–85, 1998.

[18] P-O. Persson and J. Peraire. Sub-cell shock capturing for discontinuous Galerkin methods. In *44th AIAA Aerospace Sciences Meeting and Exhibit*, page 112, 2006.

[19] D. Kuzmin. A vertex-based hierarchical slope limiter for p-adaptive discontinuous Galerkin methods. *Journal of computational and applied mathematics*, 233(12):3077–3085, 2010.

[20] K-M. Shyue and F. Xiao. An Eulerian interface sharpening algorithm for compressible two-phase flow: the algebraic THINC approach. *Journal of Computational Physics*, 268:326–354, 2014.

[21] J. Waltz, T. R. Canfield, N. R. Morgan, L. D. Risinger, and J. G. Wohlbier. Manufactured solutions for the three-dimensional Euler equations with relevance to inertial confinement fusion. *Journal of Computational Physics*, 267:196–209, 2014.

[22] Y. Lv and M. Ihme. Discontinuous Galerkin method for multicomponent chemically reacting flows and combustion. *Journal of Computational Physics*, 270:105–137, 2014.

[23] S. Galera, P-H. Maire, and J. Breil. A two-dimensional unstructured cell-centered multi-material ALE scheme using VOF interface reconstruction. *Journal of Computational Physics*, 229(16):5755–5787, 2010.

[24] A. De Brauer, A. Iollo, and T. Milcent. A cartesian scheme for compressible multimaterial models in 3D. *Journal of Computational Physics*, 313:121–143, 2016.